

# On the speckle-free nature of photoacoustic tomography

Zijian Guo, Li Li, and Lihong V. Wang<sup>a)</sup>

*Department of Biomedical Engineering, Optical Imaging Laboratory, Washington University,  
1 Brookings Drive, Saint Louis, Missouri 63130*

(Received 29 April 2009; revised 30 June 2009; accepted for publication 5 July 2009;  
published 12 August 2009)

**Purpose:** A long-standing conundrum is why photoacoustic tomography (PAT) possesses the unique ability to produce images devoid of speckle artifacts while all other coherent imaging technologies do not.

**Methods:** In this paper, we explain the inherent mechanism that suppresses speckle in PAT, and the analysis was validated by simulations based on an experimental PAT system.

**Results:** We found that the speckle-free feature of PAT results directly from the optical absorption contrast.

**Conclusions:** All optical absorbers expand on laser excitation, and therefore all initial photoacoustic pressure rises are positive, which engenders strong correlations among the photoacoustic waves from the absorbers. As a result, prominent boundaries always build up in photoacoustic images and suppress the interior speckle. © 2009 American Association of Physicists in Medicine.

[DOI: [10.1118/1.3187231](https://doi.org/10.1118/1.3187231)]

Key words: photoacoustic imaging, speckle

Speckle has been considered ubiquitous in all coherent imaging modalities, such as laser imagery,<sup>1,2</sup> ultrasonography,<sup>3,4</sup> synthetic aperture radar,<sup>5</sup> and optical coherence tomography.<sup>6</sup> Fully developed speckle is formed by the interference among partial waves, either scattered from randomly distributed scatterers or reflected from a rough surface, whose phases are completely randomized over  $2\pi$ . The speckle pattern generally has a high-contrast, fine-scale granular appearance, which does not correspond to the real structure of the sample. Although useful in certain applications, such as optical speckle imaging and ultrasound tissue characterization, speckle reduces both the effective spatial resolution and the detestability of small lesions, and thus deteriorates the image quality significantly. Many efforts have been made to mitigate this undesirable deterioration; however, speckle can be only partially reduced and only at the cost of system complexity, imaging time, or spatial resolution. Here, we explain the inherent mechanism that suppresses speckle in a novel coherent imagery: photoacoustic tomography (PAT).

Although the photoacoustic effect was first reported by Bell in 1880, PAT has only recently emerged as a promising biomedical imaging technology.<sup>7</sup> Unlike the aforementioned modalities, PAT exploits optical absorption contrast<sup>8</sup> instead of scattering contrast. Because many physiologically important molecules, such as hemoglobin, possess high characteristic absorption, PAT has provided high-quality *in vivo* images of vasculature and hemodynamic functions without the use of exogenous contrast agents.<sup>9,10</sup> More recently, the feasibility of visualizing specific molecular-related events by PAT has also been demonstrated.<sup>11</sup> In PAT, tissues are usually irradiated by a short-pulsed laser. Absorbed light is converted into heat, which is further converted to a positive pressure rise via thermoelastic expansion. The initial pressure rise then propagates as ultrasonic waves, which are detected by

ultrasonic transducers. Then, the received ultrasonic signals are used to form an image. Since ultrasound scattering is two to three orders of magnitude weaker than optical scattering in biological tissues, PAT can achieve a much better spatial resolution than traditional optical modalities beyond the optical ballistic regime ( $>1$  mm depth into the skin).

Currently, PAT has been implemented in two major forms.<sup>8</sup> One is focused-scanning PAT such as photoacoustic microscopy (PAM). One-dimensional depth-resolved photoacoustic images (A-scans) are collected by scanning a focused ultrasonic transducer. A cross-sectional or volumetric image is composed by aligning multiple A-scans at the corresponding lateral positions. The other form of implementation is photoacoustic computed tomography, in which an array of unfocused ultrasonic transducers is placed outside the object, and an image is formed using reconstruction algorithms. The following discussion is based on a reflection-mode focused-scanning PAT system developed in our laboratory,<sup>12</sup> where a 5 MHz focused ultrasonic transducer is employed. However, the linearity of PAT guarantees that the principles discussed here hold for all PAT variants.

When researchers analyze the speckle statistics in ultrasound imaging, a scattering structure is usually modeled as a collection of randomly distributed subresolution scatterers. The ultrasonic waves scattered from these scatterers interfere with each other, and speckle results. Owing to the structural continuity, the scattered waves usually possess either positive or negative polarity.

In PAT, an optically absorbing structure can be modeled as a collection of randomly distributed subresolution absorbers. The absorbers can vary in dimension widely, from hemoglobin molecules to red blood cells, as long as they are much smaller than the spatial resolution. The axial resolution of the 5 MHz PAT system, limited by the transducer band-

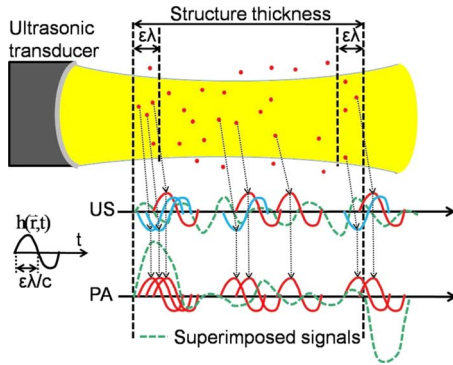


FIG. 1. Comparison of pulse-echo ultrasound imaging and reflection-mode PAT. A focused ultrasonic transducer records the A-scan signal from a slab.  $\epsilon\lambda$ , a fraction of the central acoustic wavelength  $\lambda$ ;  $c$ , speed of ultrasound. PA, photoacoustic; US, ultrasound.

width, is  $\sim 144 \mu\text{m}$ . The lateral resolution, determined by the width of the focal spot, is  $\sim 560 \mu\text{m}$ . Because an average adult has  $\sim 5 \times 10^6$  red blood cells ( $\sim 7.4\text{--}9.4 \mu\text{m}$  in diameter and  $\sim 1.6\text{--}2.0 \mu\text{m}$  in thickness) per microliter of blood, the ultrasonic transducer may receive photoacoustic waves from  $\sim 5.8 \times 10^4$  red blood cells within a resolution cell. The photoacoustic signals emitted from these absorbers interfere with each other. Curiously, investigators have noticed that photoacoustic methods, despite their coherent nature,<sup>8</sup> produce images devoid of speckle artifacts. We found that this salient feature is a direct result of the absorption contrast in PAT.

As the first explanation of the speckle-free nature of PAT, we compare a pulse-echo ultrasound imaging system with the 5 MHz reflection-mode PAT system. Both systems can be described by the same linear model. For a fair comparison without loss of generality, the same spatial-temporal system impulse response  $h(\vec{r}, t)$  is assumed for both systems. In reality,  $h(\vec{r}, t)$  in pulse-echo ultrasonography represents a round trip response, while  $h(\vec{r}, t)$  in PAT represents only one way.

Figure 1 shows that a focused ultrasonic transducer detects A-scan signals from a slab of tissue. The tissue slab is modeled as a collection of randomly distributed particles (dots), which can be either acoustic scatterers in ultrasound imaging or optical absorbers in PAT. For simplicity, we consider the particles as point targets because they are small relative to the spatial resolution. In the ultrasonic A scan, the received signals from the individual scatterers may either maintain (solid curves) or flip (dotted curves) the polarity of  $h(\vec{r}, t)$ , because the acoustic impedance of the scatterers may be either lower or higher than the surrounding medium. The photoacoustic A-scan from the absorbers of the same geometry is also plotted. Because all initial pressure rises are positive, all received photoacoustic waves uphold the polarity of  $h(\vec{r}, t)$ , which is the major difference between PAT and ultrasound imaging. The A-scan signals, plotted in dashed lines, result from the interference among the signals from the individual particles. In the middle segment of the A-scan signals in both imaging modalities, we observe random fluctuations, because of the cancellation among the positive and negative

parts of  $h(\vec{r}, t)$ . Further, the mean of the amplitudes of the fluctuations are zero because  $h(\vec{r}, t)$  does not contain a dc component (in the cases when very wideband acoustic sensors that can detect dc component are employed in PAT, we expect to see not only the boundary buildups but also the baselines inside the object). Near both the front and back boundaries, however, prominent boundary signals are observed in the photoacoustic A-scan, because of the constructive interferences. As a result, the random fluctuations in the middle are suppressed by the boundary signals, which we found to be the dominant features in photoacoustic images. By contrast, the boundary signals in ultrasound images do not stand out because of the existence of both scattering polarities. Therefore, speckle appears ubiquitously in ultrasonic A-scans.

As the second explanation, the classic speckle theory, which usually models only monochromatic waves, is invoked. As stated above, the fully developed speckle is formed by the interference of coherent waves with completely randomized phases. Two components contribute to the phase difference between waves: The initial phase and the phase delay. When profiling the central part of the structure in both photoacoustic and ultrasound imaging, we always receive acoustic waves from particles with completely randomized phases, which result from phase-delay variations. However, particles close to the boundaries send out waves that reach the transducer with approximately equal phase delays. Here, the initial phase plays a key role. As the initial photoacoustic pressure rises are always positive, the emitted photoacoustic waves add constructively to manifest the boundaries. By contrast, the scattered ultrasonic waves can take on both positive and negative initial phases. Hence, no boundary buildups are observed.

As the third explanation, we analyze the condition for building up boundaries in all coherent imaging modalities and compare the strengths of the boundaries and of the interior speckle in PAT quantitatively. Assume that a total of  $n$  particles (absorber or scatterer) are statistically uniformly distributed at positions  $\vec{r}_1, \vec{r}_2, \dots, \vec{r}_n$ . We use random process  $a_i(t)$  to denote the particle impulse response, which accounts for the properties of a single particle. Because PAT is based on the optical absorption contrast,  $a_i(t)$  depends on the optical absorption, shape, and size of the absorber.<sup>13</sup> As an absorber quickly expands on laser excitation, a strong positive initial pressure is always generated. Consequently, the early part of  $a_i(t)$  is always positive. In ultrasound imaging, as a typical scattering-based imaging modality,  $a_i(t)$  is related to the acoustic properties (density and compressibility), shape, and size of the scatterer.<sup>14</sup> In reality, the shape of  $a_i(t)$  is relatively random. The amplitude of an A scan can be written as

$$A(t) = \sum_{i=1}^n a_i(t) *_t h(\vec{r}_i, t - |\vec{r}_i|/c), \quad (1)$$

where  $*_t$  denotes convolution in the time domain and  $c$  denotes the propagation velocity of the ultrasonic wave. When Eq. (1) is applied to ultrasound imaging, round trip delays

and multiple scattering are neglected because they are not key factors in our discussions. The instantaneous power of an A-scan is  $P(t)=A^2(t)$ , and the ensemble average of  $P(t)$  becomes (see supplementary information S.1)<sup>19</sup>

$$\begin{aligned} \langle P(t) \rangle = & \rho_0 \int_V \langle \langle (a_i(t) * h(\vec{r}, t - |\vec{r}|/c))^2 \rangle \rangle_i d\vec{r}^3 \\ & + \rho_0^2 \langle b_i(t) b_j(t) \rangle_{i \neq j}, \end{aligned} \quad (2)$$

where  $b_i(t) = \langle a_i(t) \rangle * \int_V h(\vec{r}, t - |\vec{r}|/c) d\vec{r}^3$ ,  $\rho_0$  is the particle density,  $V$  is the structure volume,  $\langle \rangle_i$  is averaging over all  $n$  particles, and  $\langle \rangle_{i \neq j}$  is averaging over all particle pairs.

The first term in Eq. (2) is the sum of the powers of the waves generated from all particles. Therefore, it is called the uncorrelated contribution to the total power. It represents the power of the random fluctuations—speckle, which is shared in both imaging modalities. Speckle in ultrasound imaging has been widely used for tissue characterization.<sup>15</sup>

The second term in Eq. (2) is responsible for the prominent boundary features in photoacoustic images. Because this term represents the correlations among the particles, it is responsible for the correlated contribution to the total power. First, the correlated power appears only as boundary features, because  $\int_V h(\vec{r}, t - |\vec{r}|/c) d\vec{r}^3$  is always zero inside the structure (see supplementary information S.2 for details).<sup>19</sup> Second, the correlated power exists in photoacoustic images but usually disappears in ultrasound images. As stated above,  $a_i(t)$  in PAT always starts with a positive value, which produces strong correlations among the absorbers. After averaging over all particle pairs, the correlated power shows up as strong boundary features in PAT. In ultrasound imaging, however, the polarity of  $a_i(t)$  is relatively random. After averaging, the correlated power usually becomes negligible.

Equation (2) can be further simplified by assuming the particles to be point targets. The photoacoustic wave from each point target excited by a delta laser pulse becomes  $a_i(t) = a_i \delta'(t)$ , where each  $a_i$  is a random variable with a positive mean.<sup>16</sup> In ultrasound imaging, researchers usually assume  $a_i(t) = a_i \delta(t)$ , where each  $a_i$  is a zero mean random variable<sup>17</sup> because the scattered signal is due to fluctuations in acoustic properties relative to the mean. By substituting  $a_i(t) = a_i \delta'(t)$  or  $a_i(t) = a_i \delta(t)$  into Eq. (2), we have

$$\begin{aligned} \langle P(t) \rangle = & (\sigma_a^2 + a^2) \rho_0 \int_V (\tilde{h}(\vec{r}, t - |\vec{r}|/c))^2 d\vec{r}^3 \\ & + a^2 \rho_0^2 \left( \int_V \tilde{h}(\vec{r}, t - |\vec{r}|/c) d\vec{r}^3 \right)^2. \end{aligned} \quad (3)$$

Since integral with  $\delta'(t)$  denotes differentiation with respect to time, we have  $\tilde{h}(\vec{r}, t) = h'(\vec{r}, t)$  in PAT and  $\tilde{h}(\vec{r}, t) = h(\vec{r}, t)$  in ultrasound imaging. Here  $a$  and  $\sigma_a^2$  are the mean and variance of  $a_i$ , respectively.

From Eq. (3), we can quantify the visibility of the interior speckle in PAT, which is defined as the ratio of the square root of the average speckle power to the magnitude of boundary features, which are composed of both uncorrelated and correlated powers. The uncorrelated power is propor-

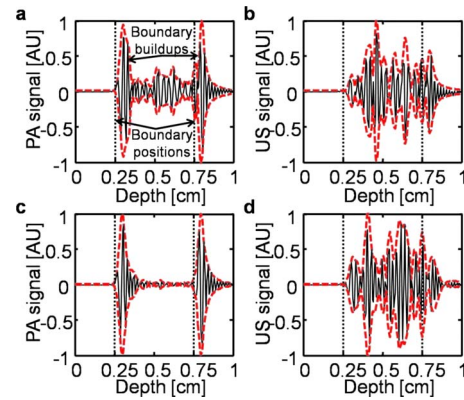


FIG. 2. Simulated depth profiles of a slab. (a) PAT, absorber density:  $1000/\lambda$ ; (b) ultrasound imaging, scatterer density:  $1000/\lambda$ ; (c) PAT, absorber density:  $100\,000/\lambda$ ; (d) ultrasound imaging, scatterer density:  $100\,000/\lambda$ .  $\lambda$ , the acoustic wavelength of 5 MHz ultrasound. PA, photoacoustic; US, ultrasound.

tional to  $\rho_0$ , while the correlated power is proportional to  $\rho_0^2$ . When  $\rho_0$  is sufficiently large, the correlated power is much stronger than the uncorrelated power, and the speckle visibility in PAT is approximately inversely proportional to  $\sqrt{\rho_0}$ . In this case, the correlated power dominates the photoacoustic image. From Eq. (3), we also note that the visibility of speckle in PAT does not depend on the particle absorbing strength, because both the correlated and uncorrelated powers are proportional to  $a^2$ . In ultrasound imaging, the second term in Eqs. (2) and (3) equals zero, and the correlated contribution is usually negligible. Therefore, the speckle visibility is independent of the scatterer density. The uncorrelated power dominates in ultrasound imaging and all other scattering-based coherent imaging modalities.

We use simulation to further illustrate our analysis. Our numerical phantom contains a 5 mm thick tissue structure, whose center is located 5 mm away from the transducer surface. It is composed of a large number of absorbers randomly distributed between 2.5 and 7.5 mm along the ultrasonic axis. The transducer is assumed to have 5 MHz central frequency with 100% bandwidth. Figure 2 compares the photoacoustic profile with the ultrasound profile, where the exact boundary positions are marked as vertical dotted lines. The envelopes represent the magnitude of absorption or scattering.

Between Figs. 2(a) and 2(b), the object has the same particle density. In the photoacoustic A-scan [Fig. 2(a)], we notice two prominent semideterministic boundaries, which dominate the random speckle fluctuations in between. The separation between either maximum profile position and the corresponding boundary position is a fraction of the center ultrasonic wavelength. In the ultrasonic A-scan [Fig. 2(b)], the speckle fluctuations spread across the entire imaged object, and no outstanding boundaries are observed.

In PAT, the visibility of the interior speckle was also found to decrease with increase in absorber density, as demonstrated in Figs. 2(a) and 2(c) and further quantified in Fig. 3(a). The linear fit between the logarithm of the speckle visibility and the absorber density has a slope of

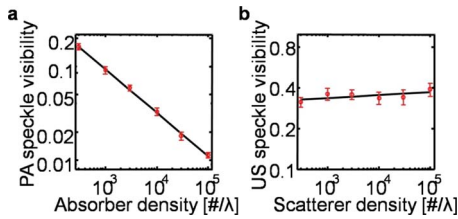


FIG. 3. Relationship between the speckle visibility in photoacoustic/ultrasound imaging and the absorber/scatterer density. (a) PAT; (b) ultrasound imaging. Error bars: Standard errors of the means (circles) based on ten realizations of particle distributions; solid lines, linear fits. PA, photoacoustic; US, ultrasound.

$-0.479 \pm 0.003$ , which is close to the inverse square-root dependence as predicted above. By contrast, the speckle visibility stays approximately constant in the ultrasound images, as illustrated in Figs. 2(b) and 2(d) and further quantified in Fig. 3(b). In both Figs. 2(a) and 2(c), each middle segment—between the two outermost minima of the profile within the two maxima—proves to be a fully developed speckle, because the magnitude of the photoacoustic signal follows the Rayleigh distribution and the intensity follows the exponential distribution. Therefore, the simulation confirms the aforementioned explanations.

In Figs. 4(a) and 4(b), we present simulated photoacoustic and ultrasonic cross-sectional images ( $B$  scan) of a round tumor, where the exact boundaries of the tumors are plotted as dashed lines. The ultrasound spatial-temporal response of the 5 MHz focused ultrasonic transducer is calculated by the FIELD II program.<sup>17</sup> We first simulate the case when the absorbing or scattering strength of the particles in the tumor area is ten times that of the background particles. For a large tumor with a diameter of 2 mm, strong signals at its top and bottom boundaries are observed in the photoacoustic  $B$  scan [Fig. 4(a)]. The side boundaries are missing due to the limited view of the linear detection geometry. Figure 4(b) shows the corresponding ultrasonic  $B$ -scan image, where speckle

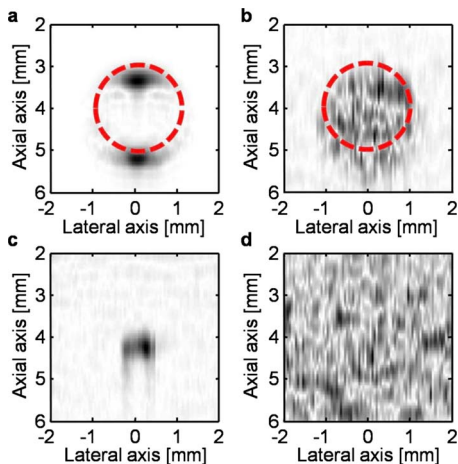


FIG. 4. Simulated cross-sectional photoacoustic and ultrasonic images of round tumors. Photoacoustic/ultrasonic  $B$  scans of tumors with [(a) and (b)] 2 mm diameter and [(c) and (d)] 100  $\mu\text{m}$  diameter. Absorber/scatterer density:  $5 \times 10^6/\mu\text{l}$ . Absorbing/scattering strength contrast: 10:1.

artifacts prevail. The higher scattering strength of the tumor induces a stronger speckle in the tumor area, which suppresses the background speckle. In reality, a 10:1 scattering strength contrast is usually unavailable in ultrasound imaging. Therefore, the background speckle may be more prominent.

In Figs. 4(c) and 4(d), respectively, the photoacoustic and ultrasonic  $B$  scans of a subresolution-sized tumor with a diameter of 100  $\mu\text{m}$  are shown. In Fig. 4(c), the small tumor appears in the photoacoustic  $B$ -scan image as a solid area without distinct front and back boundaries. In Fig. 4(d), the tumor cannot be identified in the ultrasonic  $B$ -scan image. We also simulated the case when the particle density is higher in the tumor area (see supplementary figures 1(a) and 1(b)).<sup>19</sup> As expected, the interior speckle is further suppressed in the photoacoustic image, whereas the visibility of speckle remains unchanged in the ultrasound image.

We should note that the correlated power can also exist in ultrasound imaging in rare cases. For example, the observation of correlated power at scatterer concentration gradients (boundaries) in ultrasonic  $A$  scans of a sponge slab was reported.<sup>18</sup> If the shape, size, and acoustic properties of the scatterers within the structure volume are similar, the correlation among the particle impulse responses becomes strong. As a result, the correlated power may show up at the boundaries. However, this assumption usually does not hold in real human tissue, and hence no boundary buildup occurs.

We conclude that speckle artifacts in PAT are suppressed by prominent boundary buildups. The initial all-positive photoacoustic pressure rises provide strong correlation among the absorbers, which gives rise to strong boundary buildups. While images from ultrasound imaging and all other scattering-based imaging modalities are dominated by uncorrelated power, photoacoustic images are dominated by correlated power.

The first two authors (Z.G. and L.L.) contributed equally to this paper. The authors would like to thank Meng-Lin Li, Minghua Xu, and Roger Zemp for useful discussions. This work was sponsored in part by National Institutes of Health Grant Nos. R01 NS46214 (BRP), R01 EB000712, R01 EB008085, and U54 CA136398 (NTR). L.V.W. has a financial interest in Endra, Inc., which, however, did not support this work.

<sup>a)</sup> Author to whom correspondence should be addressed. Electronic mail: lhwang@biomed.wustl.edu

<sup>1</sup>J. C. Dainty, *Laser Speckle and Related Phenomena* (Springer-Verlag, Berlin, New York, 1975).

<sup>2</sup>J. W. Goodman, *Speckle Phenomena in Optics: Theory and Applications* (Roberts, Englewood, 2007).

<sup>3</sup>C. B. Burckhardt, "Speckle in ultrasound B-mode scans," *IEEE Trans. Sonics Ultrason.* **25**, 1–6 (1978).

<sup>4</sup>R. F. Wagner *et al.*, "Statistics of speckle in ultrasound B-scans," *IEEE Trans. Sonics Ultrason.* **30**, 156–163 (1983).

<sup>5</sup>J. S. Lee, "Speckle suppression and analysis for synthetic aperture radar images," *Opt. Eng.* **25**, 636–643 (1986).

<sup>6</sup>J. M. Schmitt, S. H. Xiang, and K. M. Yung, "Speckle in optical coherence tomography," *J. Biomed. Opt.* **4**, 95–105 (1999).

<sup>7</sup>M. Xu and L. V. Wang, "Photoacoustic imaging in biomedicine," *Rev. Sci. Instrum.* **77**, 041101 (2006).

- <sup>8</sup>L. V. Wang, "Tutorial on photoacoustic microscopy and computed tomography," *IEEE J. Sel. Top. Quantum Electron.* **14**, 171–179 (2008).
- <sup>9</sup>X. Wang, Y. Pang, G. Ku, X. Xie, G. Stoica, and L. V. Wang, "Non-invasive laser-induced photoacoustic tomography for structural and functional *in vivo* imaging of the brain," *Nat. Biotechnol.* **21**, 803–806 (2003).
- <sup>10</sup>H. F. Zhang, K. Maslov, G. Stoica, and L. V. Wang, "Functional photoacoustic microscopy for high-resolution and noninvasive *in vivo* imaging," *Nat. Biotechnol.* **24**, 848–851 (2006).
- <sup>11</sup>L. Li, R. Zemp, G. Lungu, G. Stoica, and L. V. Wang, "Photoacoustic imaging of lacZ gene expression *in vivo*," *J. Biomed. Opt.* **12**, 020504 (2007).
- <sup>12</sup>K. Song and L. V. Wang, "Deep reflection-mode photoacoustic imaging of biological tissue," *J. Biomed. Opt.* **12**, 060503 (2007).
- <sup>13</sup>G. J. Diebold, T. Sun, and M. I. Khan, "Photoacoustic monopole radiation in one, two, and three dimensions," *Phys. Rev. Lett.* **67**, 3384–3387 (1991).
- <sup>14</sup>P. M. Morse and K. U. Ingard, *Theoretical Acoustics* (McGraw-Hill, New York, 1968).
- <sup>15</sup>K. K. Shung and G. A. Thieme, *Ultrasound Scattering in Biological Tissues* (CRC, Boca Raton, FL, 1993).
- <sup>16</sup>L. V. Wang and H.-I. Wu, *Biomedical Optics: Principles and Imaging* (Wiley, Hoboken, NJ, 2007).
- <sup>17</sup>J. A. Jensen and N. B. Svendsen, "Calculation of pressure fields from arbitrarily shaped, apodized, and excited ultrasound transducers," *IEEE Trans. Ultrason. Ferroelectr. Freq. Control* **39**, 262–267 (1992).
- <sup>18</sup>V. L. Newhouse and I. Amir, "Estimation of scatterer volume density near a concentration gradient," *Ultrason. Imaging* **7**, 161–171 (1985).
- <sup>19</sup>See EPAPS Document No. E-MPHYA6-36-025909 for the equation derivations and the additional figures. For more information on EPAPS, see <http://www.aip.org/pubservs/epaps.html>.